Full three-dimensional investigation of structural contact interactions in turbomachines

Mathias Legrand, Alain Batailly, Benoit Magnain, Patrice Cartraud, Christophe Pierre

Full three-dimensional investigation of structural contact interactions in turbomachines

Mathias Legrand

Structural Dynamics and Vibration Laboratory, Department of Mechanical Engineering, McGill University, 817 Sherbrooke St West, Montréal, Québec H3A 2K6, Canada

Alain Batailly

Structural Dynamics and Vibration Laboratory, Department of Mechanical Engineering, McGill University, 817 Sherbrooke St West, Montréal, Québec H3A 2K6, Canada

Benoît Magnain

ENSIB-Laboratoire PRISME, 88 boulevard Lahitolle, 18020 Bourges Cedex, France

Patrice Cartraud

LUNAM Université, GeM, UMR CNRS 6183, École Centrale de Nantes, 1 rue de la Noë, 44321 Nantes Cedex 3, France

Christophe Pierre

University of Illinois, 377 Henry Administration Building, 506 South Wright Street, Urbana, IL 61801, USA

Abstract

Minimizing the operating clearance between rotating bladed-disks and stationary surrounding casings is a primary concern in the design of modern turbomachines since it may advantageously affect their energy efficiency. This technical choice possibly leads to interactions between elastic structural components through direct unilateral contact and dry friction, events which are now accepted as normal operating conditions. Subsequent nonlinear dynamical behaviors of such systems are commonly investigated with simplified academic models mainly due to theoretical difficulties and numerical challenges involved in non-smooth large-scale realistic models. In this context, the present paper introduces an adaptation of a full three-dimensional contact strategy for the prediction of potentially damaging motions that would imply highly demanding computational efforts for the targeted aerospace application in an industrial context. It combines a smoothing procedure including bicubic B-spline patches together with a Lagrange multiplier based contact strategy within an explicit time-marching integration procedure preferred for its versatility.

The proposed algorithm is first compared on a benchmark configuration against the more elaborated bi-potential formulation and the commercial software Ansys. The consistency of the provided results and the low energy fluctuations of the introduced approach underlines its reliable numerical properties. A case study featuring blade-tip/casing contact on industrial finite element models is then proposed: it incorporates component mode synthesis and the developed 3D contact algorithm for investigating structural interactions occurring within a turbomachine compressor stage. Both time results and frequency-domain analysis emphasize the practical use of such a numerical tool: detection of severe operating conditions and critical rotational velocities, time-dependent maps of stresses acting within the structures, parameter studies and blade design tests.

Keywords: Contact dynamics; nonlinear dynamics; Lagrange multipliers; surface B-spline; modal synthesis; time-marching techniques

1 Introduction

With the endlessly growing contribution of full three-dimensional nonlinear analyses in structural components design, aircraft engine manufacturers strongly depend on the development and use of modern numerical tools. Related computational strategies traditionally based on the standard Finite Element Method routinely address structural configurations involving nonlinear kinematic descriptions, finite strains, constitutive laws with plasticity, crack propagation, nonlinear temperature gradients or unilateral contact constraints together with friction conditions, all within commercial software packages. Nevertheless, investigations requiring the enforcement of non-penetration constraints are still prone to numerical robustness issues that often necessitate in-house tools dedicated to very limited classes of problems.

In this context, the present study focuses on the development, validation and use of a 3D contact algorithm devoted to the examination of blade tips/casing structural contact interactions in modern turbomachines. These structural contacts are consequences of the implementation of improved energy efficient technologies affecting the operating clearances between the rotor and the surrounding stationary casing components potentially yielding severe damages [36, 17, 37]. Exploration of these phenomena demands meticulous attention on the considered solution method and related assumptions. Among the commonly used approaches in nonlinear dynamics (harmonic balance and shooting methods, analytical derivations and perturbation techniques, nonlinear modal analysis to name a few), time integration is given preference in the present work for its versatility and due to the complexity of the investigated phenomenon. As shown in previous studies involving 2D models [28], the forward increment Lagrange multiplier approach within an explicit time-marching technique [12] stands as a reliable strategy for this class of problems and is here extended to full 3D configurations [6]. Special consideration is given to large sliding and high tangential relative velocities between blade-tips and surrounding casings.

The novelty of the suggested approach lies in the efficient combination of several ingredients which have been already proposed for other matters:

1. construction of reduced-order models of large scale systems embedding centrifugal stiffening, *i.e.* dependence to a rotational velocity [41],

2. explicit time-stepping technique dedicated to unilateral contact and dry friction conditions,

3. contact interface smoothing procedure.

For a given blade design, the introduced numerical tool is able to provide a full cartography of its nonlinear frequency response (displacements, strains, stresses, contact forces) over a user-defined range of rotational velocities, in no more than few hours on a standard computer. By contrast, in commercial codes, centrifugal stiffening first necessitates a static pre-calculation for each investigated rotational velocity. This static computation requires a full, often very large (up to 1.5 million degrees of freedom), finite element model. The construction of reduced-order models directly embedding centrifugal stiffening significantly improves the numerical efficiency of the proposed strategy with respect to commercial softwares. The introduced tool is also versatile in such a way that existing meshing procedures implemented in industrial frameworks do not have to be modified. In this regard, consideration has been given to B-spline [10, 4, 35, 32] surface patches.

Contact problems are inherently nonlinear since the contact area is *a priori* unknown and the respective hybrid contact pressure/displacement boundary conditions are part of the sought solution. The main difficulty lies in the constitutive laws of contact and friction expressed by non-smooth multivalued force-displacement relationships. From a mechanical engineering viewpoint, three groups of methods are usually preferred for the numerical treatment of such laws since they directly provide a physical sense to the quantities of interest: (1) the penalty method [3, 24], (2) the Lagrange multiplier method [5, 21] and (3) the augmented Lagrangian method [39]. While the penalty method depends on a parameter that allows a loosely controlled violation of the constraints between the structures, the Lagrange multipliers, which represent the contact reaction forces when convergence is reached, exactly enforce the non penetration conditions.

In a FEM context, unilateral contact and friction conditions are especially challenging due to the constant switches in the state of the constraints stemming from the spatial discretization. The contact zone is represented by a surface which is only piecewise differentiable, and most commonly of low order of continuity. As a consequence, numerical jumps in contact forces are typically encountered. These non-physical jumps can cause serious errors in the resulting simulated stresses and forces and smoothing methods are often required. A higher order of continuity can be prescribed by directly using $\mathcal{C}^n$ compatible and geometrically curved elements. Unfortunately, these elements are known to feature numerical difficulties [15] that may be overcome in an original fashion. Among possible strategies that have revealed themselves useful over the past few years [29], Bézier curves, Hermite and Bernstein patches [45], Overhauser segments [1], the diffuse approximation approach [13], the B-splines [10, 4, 35, 32] and the non-uniform rational B-splines (NURBS) [42, 20] stimulated a number of interesting investigations. While preserving the original meshes, they remove the facetization issues, ease the contact transition and then increase the convergence rates of the dedicated contact algorithms. Industrial environments may greatly benefit from such implementations since they simplify meshing procedures by allowing the use of a broader class a finite elements. All these mathematical objects are characterized by their own specific advantages and drawbacks (control points interpolation, refinement, knots insertion, internal subdivision) and the Bézier and B-spline curves are the most popular forms to date. In the present study, the cubic B-spline approach is adopted since it can easily be adapted to finite element meshes where the current positions of the nodes only are required.

For reliability and validation purposes, the proposed approach is first compared against the bi-potential method [18] and the Ansys commercial package. The formulation combining augmented Lagrange multipliers with the bi-potential method is capable of treating frictional contact constraints in a reduced system by means of a predictor-corrector solution algorithm. In addition, the bi-potential method leads to a single displacement variational principle and a unique inequality in which unilateral contact and friction are coupled via a contact bi-potential. Ansys commercial software allows for several types of contact treatment. The choice essentially involves the definition of contact areas (node-to-node, node-to-surface, line-to-surface, surface-to-surface...) and the solution algorithm (multipoint constraint, penalty, Lagrange multiplier or augmented Lagrangian methods). Each contact simulation is customizable with a large number of parameters. In our study, CONTA175 and TARGE170 [2] are used to define node-to-surface 3D contact areas and the solution is computed with the augmented Lagrangian procedure. The targeted application case, depicted in Fig. 1, is presented in the last section.
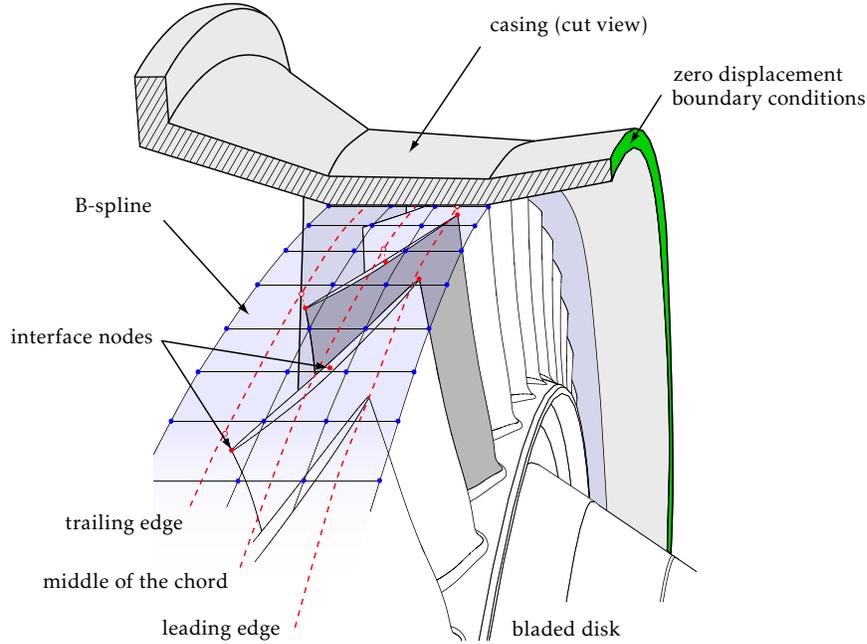
Figure 1: Surface-spline description for treatment of contact conditions between blade-tips and surrounding casing in turbomachinery

2 Contact dynamics

2.1 General theory

The contact pressure acting between the blade tips and the casing is of particular interest in this study. Equations of motion are derived using the Principle of Virtual Work within the kinematically linear framework following reference [27]. The infinitesimal strain theory is assumed and the reference frame is attached to the rotating blade.

It is first convenient to arbitrary choose a master surface, subjected to contact, with respect to which a second one, commonly called the slave surface, can be parameterized. It is then possible to find for any material point $\mathbf{x}$ belonging to the master surface $\Gamma_c^{(m)}$, its closest counterpart $\bar{\mathbf{y}}$ on the slave surface $\Gamma_c^{(s)}$:

$$\bar{\mathbf{y}}(\mathbf{x}) = \arg\min_{\mathbf{y}\in\Gamma_c^{(s)}} \|\mathbf{x} - \mathbf{y}\| \tag{1}$$

According to these notations, the gap function between the two structures can be expressed:

$$g(\mathbf{x}) = g_0(\mathbf{x}) + \left(\mathbf{u}^{(m)}(\mathbf{x}) - \mathbf{u}^{(s)}(\bar{\mathbf{y}}(\mathbf{x}))\right) \cdot \mathbf{n} \tag{2}$$

where $g_0(\mathbf{x})$ represents the initial positive gap between the two structures, $\mathbf{n}$, the outward normal to $\Gamma_c^{(s)}$, and $\mathbf{u}$, the displacement of the master $^{(m)}$ and slave $^{(s)}$ structures. The contact conditions, referred to as the Kuhn-Tucker optimality conditions are such that for all $\mathbf{x}\in\Gamma_c^{(m)}$:

$$t_N \geq 0, \quad g \geq 0, \quad t_N g = 0 \tag{3}$$

where t_N stands for the positive contact pressure acting on $\Gamma_c^{(m)}$. These conditions are

4

complemented by the Coulomb friction law:

$$
\begin{aligned}
&\|\mathbf{t_T}\| \leq \mu t_N \\
&\|\mathbf{t_T}\| < \mu t_N \Rightarrow \mathbf{v_T} = 0 \\
&\|\mathbf{t_T}\| = \mu t_N \Rightarrow \exists\, \alpha > 0 \text{ such as } \mathbf{v_T} = \alpha \frac{\mathbf{t_T}}{\|\mathbf{t_T}\|}
\end{aligned}
\tag{4}
$$

for which μ is the coefficient of friction, $\mathbf{v_T}$, the tangential slip and $\mathbf{t_T}$, the tangential stress vector. The weak form of the contact problem can be then written in the following manner:

find the displacement field $\mathbf{u}$ such as for all admissible virtual displacement $\delta\mathbf{u}$:

$$
\begin{aligned}
\int_{\Omega} \rho\ddot{\mathbf{u}} \cdot \delta\mathbf{u}\,\mathrm{d}V + \int_{\Omega} \bar{\bar{\sigma}} : \delta\bar{\bar{\varepsilon}}\,\mathrm{d}V &= \int_{\Gamma_\sigma} \mathbf{t_d} \cdot \delta\mathbf{u}\,\mathrm{d}S + \int_{\Gamma_c^{(s)}} (t_N \delta g + \mathbf{t_T} \cdot \delta\mathbf{u_T})\,\mathrm{d}S \\
&+ \int_{\Omega} \mathbf{f_d} \cdot \delta\mathbf{u}\,\mathrm{d}V
\end{aligned}
\tag{5}
$$

where t_N and $\mathbf{t_T}$ should satisfy conditions (3) and (4), respectively. The virtual work of the contact forces is calculated on the slave surface $\Gamma_c^{(s)}$, in other words, the surface spline attached to the casing. It means that the gap functions are evaluated using the surface spline — and not the original casing mesh — and that the virtual displacements of the interface nodes due to the contact forces acting on the surface spline are calculated using the shape functions of the surface spline together with the inversion procedure between data and control point detailed in Eqs (23) and (25).

2.2 Solution algorithm for interaction

Many different time-marching procedures dealing with contact have been developed in the past few years depending on the type of correction used (displacement or velocity) [43]. Because of its simplicity, the Forward Increment Lagrange Multiplier Method [12] is used in our study. The matrix form of (5) is discretized in time using the explicit central differences scheme. The algorithm is then divided into three steps:

1. **prediction** at time step $n+1$ of the displacements $\mathbf{u}$ of the structures without considering any contact. This predicted displacement, denoted with a superscript ^{p}, is analytically expressed as:

$$
\mathbf{u}^{n+1,p} = \left[\frac{\mathbf{M}}{h^2} + \frac{\mathbf{D}}{2h}\right]^{-1} \left(\left(\frac{2\mathbf{M}}{h^2} - \mathbf{K}\right)\mathbf{u}^n + \left(\frac{\mathbf{D}}{2h} - \frac{\mathbf{M}}{h^2}\right)\mathbf{u}^{n-1} + \mathbf{F}^n\right)
\tag{6}
$$

where h is the time-step size of the explicit time marching procedure. Previous displacements $\mathbf{u}^n$ and $\mathbf{u}^{n-1}$ and external forcing $\mathbf{F}^n$ are known.

2. **determination** of the gap function vector $\mathbf{g}^p$ between the two structures using Eq. (2). Each gap function where a penetration has been detected is kept in $\mathbf{g}^p$, all other coordinates of the latter being zero.

3. **correction** of the displacements through the calculation of the Lagrange multipliers. This step implies that the gap functions (linearized when necessary) vanish:

$$
\mathbf{g}^{n+1} = \mathbf{C_N}^t\mathbf{u}^{n+1,c} + \mathbf{g}^p = \mathbf{0}
\tag{7}
$$

where the superscript ^{c} means that the correction of the displacements is being calculated. $\mathbf{C_N}$ is the contact constraint matrix in the normal direction where superscript ^{t} stands for *transpose*. The new equations of motion taking the Lagrange

multipliers (i.e. contact forces) into account and the contact constraints have to be solved simultaneously. To this end, a new contact matrix $\mathbf{C_{NT}}$ containing the normal and tangential constraints is built by considering that, because of high relative velocities between the two structures, only sliding occurs:

$$
\begin{cases}
\lambda = \left(\mathbf{C_N}^t \left[\dfrac{\mathbf{M}}{h^2} + \dfrac{\mathbf{D}}{2h} \right]^{-1} \mathbf{C_{NT}} \right)^{-1} \mathbf{g}^p \\[3mm]
\mathbf{u}^{n+1} = \mathbf{u}^{n+1,p} + \left[\dfrac{\mathbf{M}}{h^2} + \dfrac{\mathbf{D}}{2h} \right]^{-1} \mathbf{C_{NT}} \lambda
\end{cases}
\tag{8}
$$

4. **time increment** $t \leftarrow t + h$ and go back to 1.

3   Smoothing procedure

The usual mathematical inconsistencies in contact treatment due to the finite element mesh approximation — i.e. exact distances between the two structures and continuous definition of the outward normal direction — is overcome through the implementation of a functional smoothing procedure of the contact surface involving bi-cubic B-splines [4], as pictured in Fig. 1.

3.1   B-spline curves

3.1.1   Uniform B-spline curve

B-spline bases [11] allow the construction of complex parametric spatial curves $\mathbf{c}(t)$ by multiplying a spline basis functions $B_{ni}(t)$ and a set of control points $\mathbf{Q}_i$[1]:

$$
\mathbf{c}(t) = \sum_{i=0}^{N-1} \mathbf{Q}_i B_{ni}(t)
\tag{9}
$$

They result by mapping a dimension t defined along a knot sequence $t_{i=0,N-1}$ into a Cartesian space through control points and are completely specified by the curve's control points, the curve's polynomial degree and the B-spline basis functions as detailed in Eq. (9).

Two-dimensional splines will be later employed to enrich the contact surface functional properties. This surface will be characterized by its degree n and the knot sequence characterized by the following considerations:

- Choosing $n = 3$ provides a C^1 continuity to the normal of the contact surface, which is of primary importance to correctly calculate the distance between the structures and to avoid numerical jumps in the estimation of the contact forces. Lower degree polynomials do not provide sufficient control of the surface's shape and higher degree polynomials are computationally more expensive.

- The knot sequence can be either uniform or nonuniform. A curve is uniform if the spacing between the knots of the intrinsic parameter t is constant, $t_{i+1} = t_i + 1$. This method is not always suitable and chord length parametrization may be preferred

---

[1]In a three-dimensional Cartesian space, the parametric curve is a vector-valued function of parameter t such as $\mathbf{c}(t) = [c_x(t), c_y(t), c_z(t)]$. The control points are stored accordingly along the three directions such as $\mathbf{Q}_i = [Q_{xi}, Q_{yi}, Q_{zi}]$.

because it more precisely reflects the geometry of the data points by proportion-ally spacing the knot sequence to the distance between the data points. However, the contact interface nodes of the casing supporting the surface spline are (almost) equally spaced along the circumferential and axial directions (see Fig. 1). More-over, a uniform parametrization greatly simplifies the implementation.

Consequently, *cubic uniform* B-spline curves are used in the present study. Each segment p of the curve[2] can be then written in a matrix form:

$$c_p(t) = \mathbf{TMQ}_p \tag{10}$$

where $\mathbf{T} = (t^3, t^2, t, 1)$, $\mathbf{Q}_p^t = (Q_{p-1}, Q_p, Q_{p+1}, Q_{p+2})$ and:

$$\mathbf{M} = \frac{1}{6}\begin{bmatrix} -1 & 3 & -3 & 1 \\ 3 & -6 & 3 & 0 \\ -3 & 0 & 3 & 0 \\ 1 & 4 & 1 & 0 \end{bmatrix} \tag{11}$$

3.1.2 Interpolation

By definition, a B-spline does not pass through its control points. The inversion method addresses this issue by finding the $N + 2$ control points Q_i, given a set of N data points P_i to be interpolated. N linear equations are generated based on the fact that $c(t)$ has to pass through the data points. This generates a spline which will (almost) perfectly match the geometry of the supporting casing.

In the case of a uniform parametrization, segment p of the spline curve reaches its extremal points P_p and P_{p+1} for extremal values of parameter t, respectively $t = 0$ and $t = 1$. Accordingly, it yields for $p = 0, \ldots, N - 2$:

$$
\begin{aligned}
P_p &= c_p(0) = \frac{1}{6}\left(Q_{p-1} + 4Q_p + Q_{p+1}\right) \\
P_{p+1} &= c_p(1) = \frac{1}{6}\left(Q_p + 4Q_{p+1} + Q_{p+2}\right)
\end{aligned}
\tag{12}
$$

where $c_p(1) = c_{p+1}(0)$. System (12) can be recast in a matrix form such as:

$$
\begin{pmatrix} \text{end 1} \\ P_0 \\ P_1 \\ \\ \vdots \\ \\ P_{N-2} \\ P_{N-1} \\ \text{end 2} \end{pmatrix} = \frac{1}{6}\begin{bmatrix} \text{e n d c o n d i t i o n s 1} \\ 1\ 4\ 1\ 0 & \cdots & 0 \\ 0\ 1\ 4\ 1\ 0 & \cdots & 0 \\ \vdots & \ddots & \vdots \\ 0 & \cdots & 0\ 1\ 4\ 1\ 0 \\ 0 & \cdots & 0\ 1\ 4\ 1 \\ \text{e n d c o n d i t i o n s 2} \end{bmatrix}\begin{pmatrix} Q_{-1} \\ Q_0 \\ Q_1 \\ \vdots \\ Q_{N-2} \\ Q_{N-1} \\ Q_N \end{pmatrix} \tag{13}
$$

or, in a contracted way:

$$\mathbf{P} = \mathbf{AQ} \tag{14}$$

where the two end-conditions required to uniquely solve the problem have to be speci-fied.

---

[2]As already mentioned, a curve is generally vector-valued but is written here along a single direction of the Cartesian space for the sake of simplicity.

3.1.3 End Conditions

Various methods are available for the definition of the boundary and end-conditions — both a 2D and a 3D representation of two possible end-conditions are given in Figs. 2, 3(a), and 3(b) — of an interpolating spline patch. In the perspective of the casing problem, two types of end-condition should be explored: free edges along the axial direction of the structure as well as continuity and closure conditions along the circumferential direction. The first one is dealt with the double vertice approach [7, 4]:

$$Q_{-1} = Q_0 \quad \text{and} \quad Q_N = Q_{N-1} \tag{15}$$

which assumes that the curvature of the spline curve at each end is zero. The second one requires the position of the spline $c(t)$, its first $c(t)'$, and second $c(t)''$ spatial derivatives to be equal at extremities in order to enforce closure and functional smoothness, mathematically leading to:

$$
\begin{aligned}
c_0(0) = c_{N-2}(1) &\Leftrightarrow P_0 = P_{N-1} \\
c_0'(0) = c_{N-2}'(1) &\Leftrightarrow -Q_{-1} + Q_1 = -Q_{N-2} + Q_N \\
c_0''(0) = c_{N-2}''(1) &\Leftrightarrow Q_{-1} - 2Q_0 + Q_1 = Q_{N-2} - 2Q_{N-1} + Q_N
\end{aligned}
\tag{16}
$$

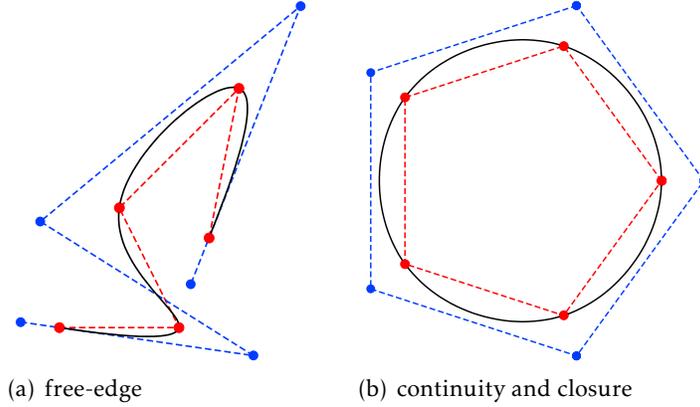Finally, in Eq. (13), free edge boundary conditions in the axial direction read:

(a) free-edge   (b) continuity and closure

Figure 2: two types of end condition: spline (——), data points $\mathbf{P}$ (•) and control points $\mathbf{Q}$ (•)

$$
\begin{aligned}
\text{end conditions } 1 &= [1 \; -1 \; 0 \; \dots \; 0] \\
\text{end conditions } 2 &= [0 \; \dots \; 0 \; -1 \; 1]
\end{aligned}
\tag{17}
$$

and continuity boundary conditions in the circumferential direction are:

$$
\begin{aligned}
\text{end conditions } 1 &= [-1 \; 0 \; 1 \; 0 \; \dots \; 0 \; 1 \; 0 \; -1] \\
\text{end conditions } 2 &= [1 \; -2 \; 1 \; 0 \; \dots \; 0 \; -1 \; 2 \; -1]
\end{aligned}
\tag{18}
$$

3.2 Bicubic uniform B-spline surfaces

3.2.1 Construction

B-spline surfaces are an extension of B-spline curves and are most commonly defined as the tensor product of B-spline curves:

$$\mathbf{S}(s,t) = \sum_{i=0}^{M-1} \sum_{j=0}^{N-1} \mathbf{Q}_{ij} B_{ni}(s) B_{nj}(t) \tag{19}$$

involving two parametric values s and t defined on two knot vectors (s_i) and (t_j), and a set of control points $\mathbf{Q}_{ij}$, organized in a grid and thus, not of arbitrary topology. Accordingly, the surface basis functions are products of two univariate bases. Similar to the uniform cubic B-spline curve, $\mathbf{S}(s,t)$ is a vector-valued function and each patch[3] pq of a bicubic uniform B-spline surface can be described in a matrix form by:

$$S_{pq}(s,t) = \mathbf{SMQ}_{pq}\mathbf{M}^t\mathbf{T}^t \tag{20}$$

with $\mathbf{S} = (1,s,s^2,s^3)$, $\mathbf{T} = (1,t,t^2,t^3)$ and:

$$\mathbf{Q}_{pq} = \begin{bmatrix} Q_{p-1,q-1} & Q_{p-1,q} & Q_{p-1,q+1} & Q_{p-1,q+2} \\ Q_{p,q-1} & Q_{p,q} & Q_{p,q+1} & Q_{p,q+2} \\ Q_{p+1,q-1} & Q_{p+1,q} & Q_{p+1,q+1} & Q_{p+1,q+2} \\ Q_{p+2,q-1} & Q_{p+2,q} & Q_{p+2,q+1} & Q_{p+2,q+2} \end{bmatrix} \tag{21}$$

where matrix $\mathbf{M}$ is defined in Eq. (11). As shown in Eqs. (20) and (21), each bicubic uniform B-spline patch is locally affected by sixteen control points.

3.2.2 Interpolation

For the sake of simplicity $\mathbf{Q}$ (respectively $\mathbf{P}$) now denotes a reorganization of matrix $\mathbf{Q}_{pq}$ given in Eq. (21) (respectively $\mathbf{P}_{pq}$) for $p = -1,\ldots,M$ and $q = -1,\ldots,N$ in a vector form such as:

$$\begin{aligned} \mathbf{Q}^t &= (Q_{-1-1},Q_{0-1},\ldots,Q_{M-1},Q_{-10},Q_{00},\ldots,Q_{MN}) \\ \mathbf{P}^t &= (P_{-1-1},P_{0-1},\ldots,P_{M-1},P_{-10},Q_{00},\ldots,P_{MN}) \end{aligned} \tag{22}$$

The two dimensional counterpart of Eq. (14) together with notations (22) and the appropriate end-conditions into Eq. (19) (see Fig. 3(b)) leads to the following relation between data and control points:

$$\mathbf{P} = \mathbb{A}\mathbf{Q} \tag{23}$$

where matrix $\mathbb{A}$, of size $\left((N+2)\times(M+2)\right)^2$, is defined as the Kronecker product of matrices $\mathbf{A_s}$ and $\mathbf{A_t}$, counterparts of matrix $\mathbf{A}$ of Eq. (14) with the appropriate end-conditions, respectively in s and t:

$$\mathbb{A} = \mathbf{A_s} \otimes \mathbf{A_t} \tag{24}$$

whose inversion is:

$$\mathbb{A}^{-1} = \mathbf{A_s}^{-1} \otimes \mathbf{A_t}^{-1} \tag{25}$$

In the validation example as well as in the application case, matrix $\mathbf{P}$ contains the actual nodes of the finite element mesh on the contact surface. This means that every time the B-spline surface is created, control points $\mathbf{Q}$ are computed so that nodes in $\mathbf{P}$ belong to the B-spline surface.

---

[3]two-dimensional counterpart of a segment, written here in one direction of the Cartesian space

(a) free-edge end-conditions and compatibility in displacement (closure)

(b) continuity conditions (first and second spatial derivatives) and compatibility in displacement (closure)

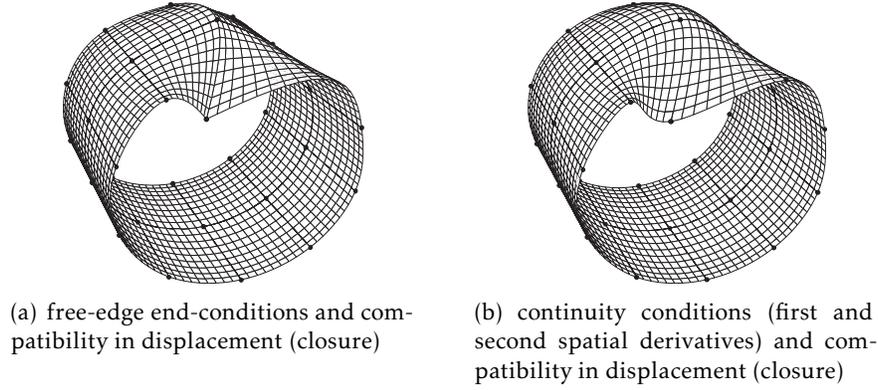Figure 3: Surface spline versus end-conditions along the circumferential direction. Free-edge end-conditions in the axial direction. Black dots • are the data points of the deformed casing. The control points and vertices are not shown.

4 General algorithm validation

As explained in the introduction, exploration of blade-to-casing interactions involves numerical difficulties due to unilateral contact conditions and high relative velocities. Accordingly, it is important to validate the developed in-house numerical tool by comparing results to the existing software packages and other academic codes on specific configurations designed to asymptotically approximate a blade-to-casing interaction. The comparison is addressed with the bi-potential method [18] combined with an implicit time integration procedure and the Ansys commercial software. The respective contact example is presented in Fig. 4 and a summary of the considered solution methods is provided in Tab. 1.

Solution method	Time integration method	Contact algorithm	Contact surface interpolation
Proposed algorithm	explicit	Lagrange multiplier	B-splines
Bi-potential	implicit	Augmented Lagrangian	Linear
Ansys	implicit	Augmented Lagrangian	Linear

Table 1: Solution methods

4.1 Benchmark configuration

A flexible cubic hexahedron is launched between two flexible partial rings clamped on their tip boundaries. The initial velocity of the hexahedron $\mathbf{v}_c$ is directed along the $\mathbf{y}$ axis. Positions C_l and C_r define the centers of the left partial ring ($x < 0$) and right partial ring ($x > 0$).

In the sequel, subscripts $_r$ and $_h$ respectively refer to the rings and the hexahedron. The mechanical parameters common to all subsequent numerical simulations are as follows: Young's modulii $E_r = 2.1 \cdot 10^{11}$ N/m^2 and $E_h = 2.1 \cdot 10^9$ N/m^2, mass per unit volume $\rho_r = \rho_h = 7{,}800$ kg/m^3 and Poisson coefficients $\nu_r = \nu_h = 0.3$. Structural damping and gravity are neglected. Structures are meshed with 8-node linear brick elements. The cube is discretized with 125 identical elements (5 elements on each length) and the rings are regularly meshed with 5 elements along their thickness, 8 elements along
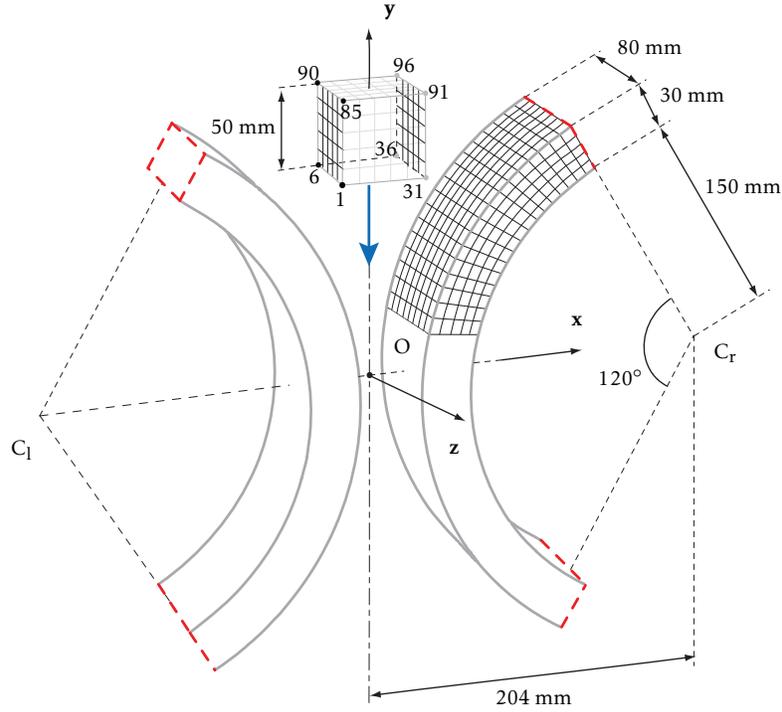
Figure 4: Benchmark configuration

their width and 40 elements along their length, so that each ring is discretized in 1,600 elements.

Within the linear kinematic framework, it seems legitimate to restrict the contact conditions to two faces of the hexahedron, respectively delimited by nodes 1, 85, 90 and 6 and by nodes 31, 91, 96 and 36, as pictured in Fig. 4.

Finally, for each ring, a B-spline surface is attached to the nodes of the outer surface of the ring as detailed in section 3. Free edge conditions only are considered and the B-spline surface matches the outer surface of each ring mesh.

4.2   Displacements and contact forces

The investigated design is symmetric with respect to planes ($O\mathbf{yz}$) and ($O\mathbf{yx}$) and it is expected to observe symmetric displacements and contact forces. This is verified by comparing u_x, u_y and u_z for nodes 1, 6, 85 and 90 with their respective symmetric counterparts on nodes 31, 36, 91 and 96 as pictured in Fig. 4.

Figs. 5(a), 5(b), 5(c) and 5(d) show perfect symmetry for both displacements and contact forces with indistinguishable superimposition.

4.3   Sensitivity to friction

With the same boundary and initial conditions, three configurations are investigated for various friction coefficients μ and initial velocities $\|\mathbf{v}_c\|$ in order to assess the sensitivity to assumptions listed in section 2.2. Constant time step is $h = 10^{-7}$ s in the proposed technique and $h = 10^{-5}$ s, in the bi-potential method.
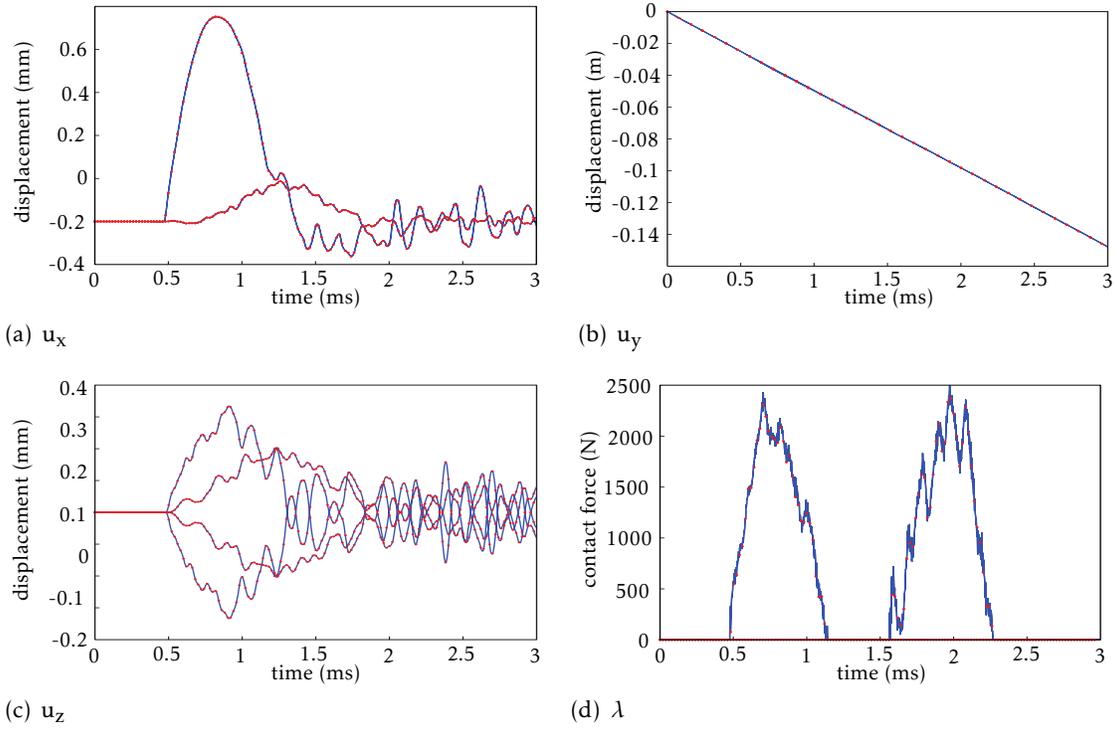
11

(a) u_x

(b) u_y

(c) u_z

(d) λ

Figure 5: Displacements and contact force for nodes 1, 6, 85 and 90 (——)
and their respective symmetric: nodes 31, 36, 91 and 96 (········)

4.3.1 $\mu = 0$

The initial speed of the cube is -50 m/s for the first two configurations. With its initial velocity, the hexahedron stores a sufficiently high kinetic energy to distort itself as well as the two flexible rings, and thus entirely moves through the existing clearance.

A comparison between the proposed algorithm and the bi-potential method is conducted for displacements and contact forces. For the sake of brevity, the results are only presented for node 1 of the hexahedron. As shown in Fig. 4, the maximum relative displacement of node 1 is about 2 mm, equivalent to a 4%-strain ratio compatible with the linear kinematic assumption. Displacements u_{1x}, u_{1y}, and u_{1z} of node 1 are displayed in Figs. 6(a), 6(b), and 6(c), respectively. The contact force acting on this node is depicted in Fig. 6(d). Each figure shows a good agreement between the two methods, both in displacement and force amplitudes even though a phase shift is noticeable for u_{1x} and u_{1z}. The latter arises when the hexahedron leaves the rings behind and is strongly dependent on the initial displacement conditions of this stage. Moreover, both methods feature a decay of u_{1y} as pictured in Fig. 6(b), caused by the contact with the rings and consequence of the partial transformation of the initial kinetic energy into strain energy.

4.3.2 $\mu = 0.15$

The friction coefficient is now set to a value corresponding to experimental blade/casing set-ups. Respective displacements u_{1x}, u_{1y}, and u_{1z} are displayed in Figs. 7(a), 7(b), and 7(c). The contact force acting on this node is illustrated in Fig. 7(d). Due to dry friction during the contact phase, the velocity of the moving hexahedron decreases until the structure reaches a static position with final adherence to the surrounding rings. This
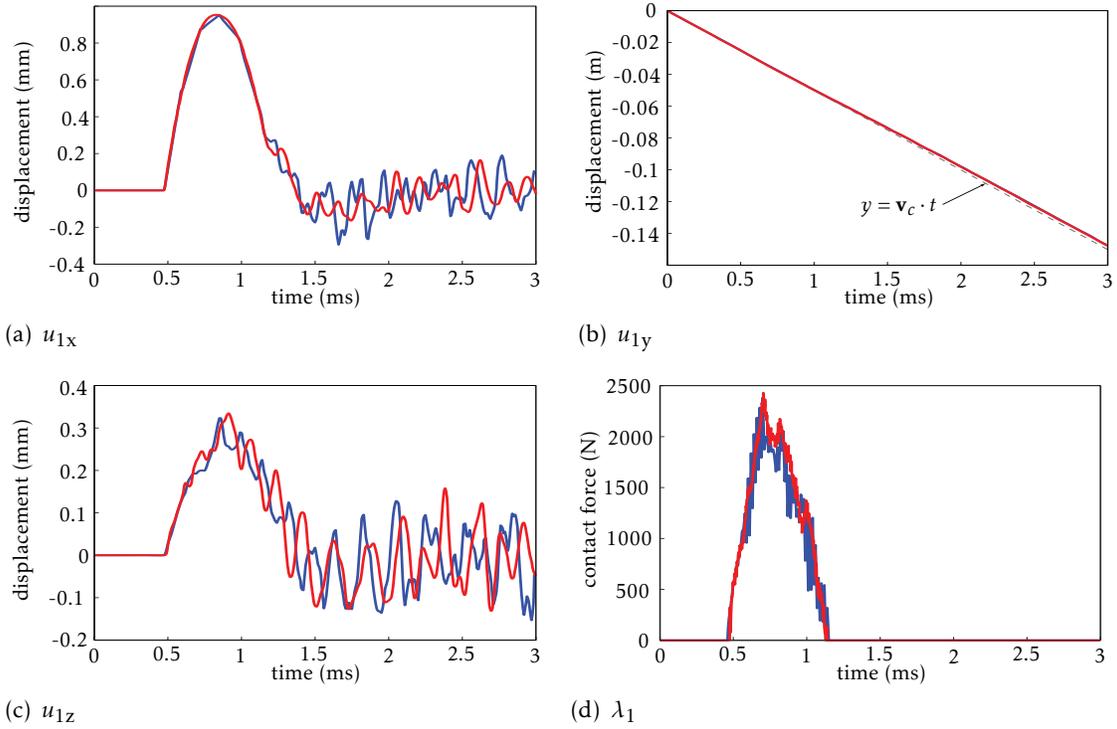
12

(a) u_{1x}

(b) u_{1y}

(c) u_{1z}

(d) λ_1

Figure 6: Frictionless low speed configuration; proposed algorithm (———)
and bi-potential method (———)

is indicated in Fig. 7(b) where the **y**-displacement becomes constant after the transient response. While Figs. 7(a) and 7(c) match very well, Fig. 7(b) shows that the hexahedron penetrates further between the rings according to the bi-potential method. This is a consequence of the contact treatment in the proposed approach only accounting for sliding (see Eq.(8)) as follows:

$$\|\mathbf{t_T}\| = \mu t_N \tag{26}$$

When the relative tangential velocity between the mechanical components is sufficiently low to allow a sticking state, the proposed method overestimates tangential contact forces.

4.4 Sensitivity to relative tangential velocity

The velocity of the hexahedron is now sufficiently high to ensure a complete sliding motion between the two rings followed by a final release. This configuration is intended to reflect the contact conditions of the blade-to-casing interaction.

Comparison for displacement of node 1 is provided in Figs. 8(a), 8(b), and 8(c). Respective contact force comparison is displayed in Fig. 8(d). In Fig. 8(b), identical behaviours in the **y** direction can be observed and the two methods predict the same cube velocity after the contact phase with the surrounding rings. Also, high frequency vibrations of significant but similar amplitude are noticeable for u_{1x} and u_{1z} in Figs. 8(a) and 8(c) due to the absence of damping.
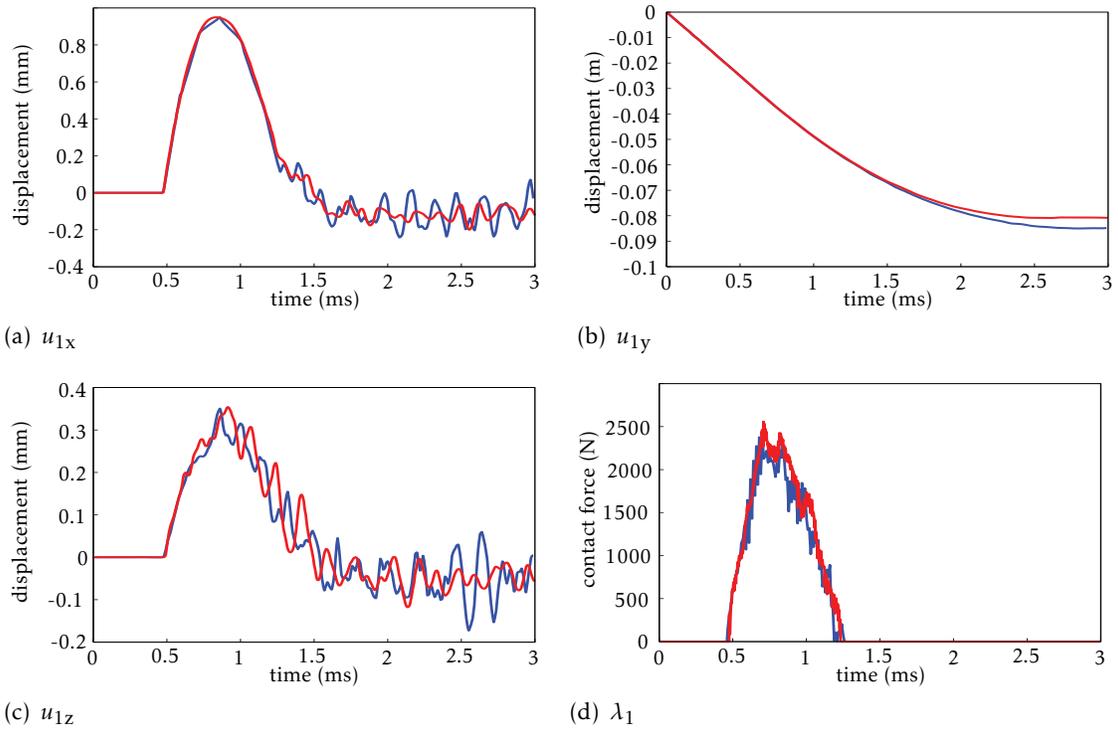
13

(a) u_{1x}

(b) u_{1y}

(c) u_{1z}

(d) λ_1

Figure 7: Low speed configuration with friction; proposed algorithm (———) and bi-potential method (———)

(a) u_{1x}
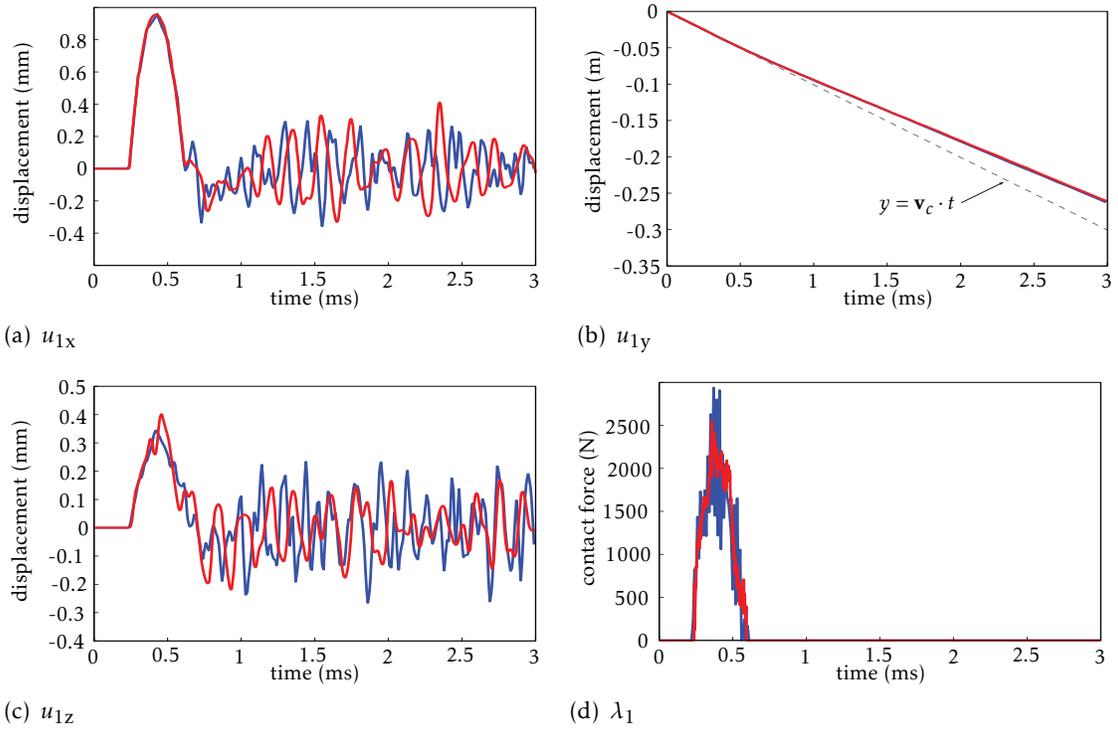
(b) u_{1y}

(c) u_{1z}

(d) λ_1

Figure 8: High speed configuration with friction; proposed algorithm (———) and bi-potential method (———)

14

4.5 Comparison to Ansys

Comparison to Ansys is introduced for the third configuration involving friction and high relative velocity.

Ansys instructions CONTA175 and TARGE170 [2] are used to define node-to-surface 3D contact interface[4]. Elements TARGE170 model the contact surface of each ring and elements CONTA175 describe the cube as pictured in Fig. 9. Ansys offers the aug-
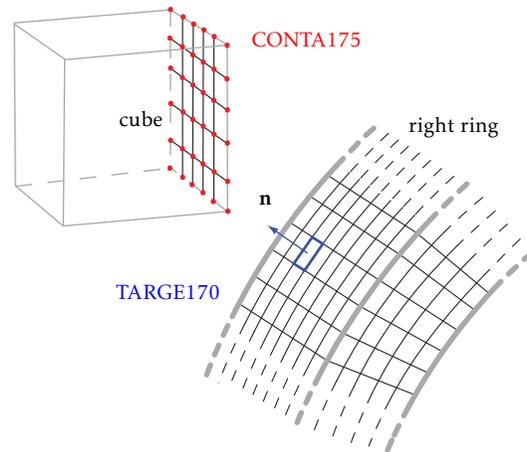

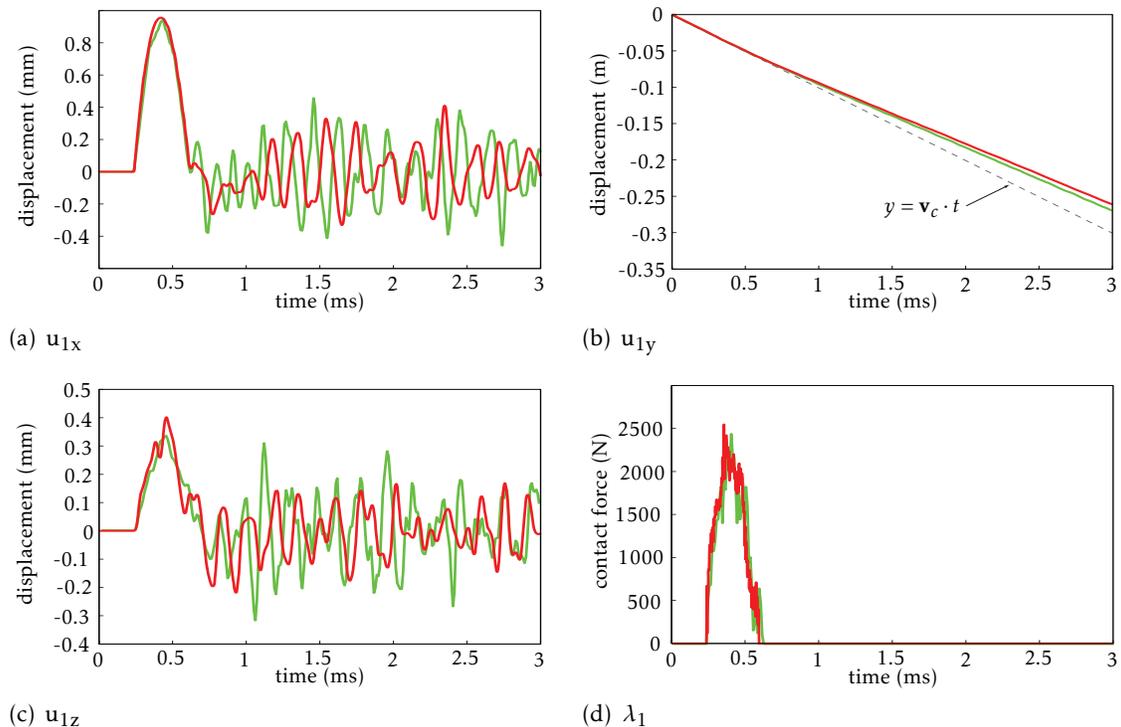Figure 9: Ansys elements used for contact simulation, partial representation of the contact case

(a) u_{1x}

(b) u_{1y}

(c) u_{1z}

(d) λ_1

Figure 10: High speed with friction, comparisons between the proposed algorithm (———) and Ansys (———)

---

[4]CONTA175 and TARGE170 elements essentially define the contact nodes and respective contact surfaces in the context of a usual master/slave approach with node-to-surface contact algorithm.

mented Lagrangian method within an implicit time integration procedure with New-mark parameters $\gamma = \frac{1}{2}$ and $\beta = \frac{1}{4}$. Time step may vary during the numerical simulation from $h_{\min} = 10^{-6}$ s to $h_{\max} = 10^{-5}$ s.

Similarly to the comparison with the bi-potential method, results match very well during the contact phase (see Fig. 10); contact forces pictured in Fig. 10(d) emphasize this statement. Once contact is released between the hexahedron and the two flexible rings (for $t > 0.6$ s), high frequency vibrations arise as displayed in Figs. 10(a) and 10(c) where both approaches lead to comparable mean amplitudes. As mentioned earlier, a phase shift is also noticeable. On the contrary, the superimposition of u_{1x} from Ansys and the bi-potential method plotted in Fig. 11 highlights a better agreement between the two strategies. There is a known delay between implicit and explicit time integra-
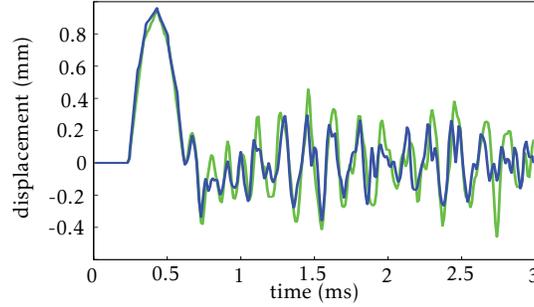

Figure 11: Displacement u_{1x} with high relative velocity and friction; Ansys (———) and bi-potential method (———)

tion procedures [19] that may be responsible for a phase shift between the respective responses. Second — and this is a critical point in our study — while the contact surface is exactly the same for simulations carried out with Ansys and the bi-potential method, a bicubic B-spline is used for interpolating the contact surface of the rings. Accordingly, the time range for which contact is released may not be exactly identical.

4.6   Energy conservation

Explicit time-stepping procedures are known to be conditionally stable with a critical time step. Such integration schemes should satisfy stability, convergence, and consistency properties as well as preserve system invariants such as linear momentum and total energy balance [27, 22]. The design of nonlinear stable algorithms satisfying conservative laws has already been widely studied on a variety of configurations [40, 34, 46, 33] and energy conserving algorithms have been developed for different applications [23, 30, 18]. The explicit central difference method ensures the conservation of the linear momentum [26] and we now focus on energy preserving properties of the proposed solution method. Since the configuration of interest is conservative when $\mu = 0$, the total energy of the system E_T should be constant. When $\mu > 0$, friction induces dissipation and the total energy of the system decreases during the sliding contact phases of the predicted motion. The energy balances the two low relative speed cases are depicted in Fig. 12(a) and 12(b). The total energy of the system is computed as the sum of the kinetic energy and the strain energy of the cube and the rings. The system total energy fluctuations are found to be very small, from 1,218.75 J to 1,216.83 J, or equivalently a 0.16 % decrease. On the contrary, the kinetic energy, and subsequently, the total energy of the system are clearly affected by friction. Accordingly, the method possesses reliable energy conservation properties which makes it well suited for long time runs of non-linear regimes.
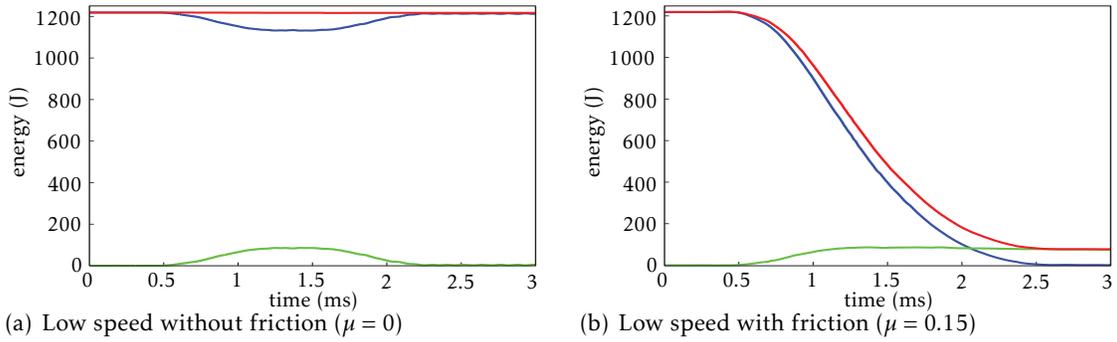
16

(a) Low speed without friction ($\mu = 0$) (b) Low speed with friction ($\mu = 0.15$)

Figure 12: Total (———), kinetic (———), and strain (———) energies versus time

The good agreement on displacements and contact forces between the three investigated approaches together with the offered energy conserving properties validate the proposed approach. Accordingly, the introduced numerical proved to be relevant for the numerical exploration of blade-tip/casing interaction in aircraft engines.

5   Analysis of a practical example

Note: in this section, numerical values are normalized. Stresses in section 5.6 are given as a percentage of the elastic limit of the blade material.

5.1   Structural models and strategy

The compressor stage of interest is partially depicted in Fig. 1. Its total diameter is 500 mm and it is constituted of 56 sectors. The bladed disk is perfectly balanced and tuned and gyroscopic effects are neglected. The green circumferences in Fig. 1 show where zero-displacement boundary conditions are prescribed. The bladed disk is supported by a perfectly rigid shaft, *i.e.* its axis of rotation does not move. For illustration purposes, a single blade only is considered with an associated 70,000 degree-of-freedom finite element model. The blade foot is clamped which means that the disk dynamics are neglected in this example.

It was experimentally shown that the casing is structurally insensitive to the interaction with the rotating blade which features much higher vibratory levels. Accordingly, the casing is considered as a rigid body statically distorted to initiate contact and interaction. Structural damping is introduced in the bladed disk through a modal damping ratio $\xi = 0.005$.

The casing internal radius is 501 mm. It is 150 mm wide in the axial direction with a 6 mm thickness. It is clamped along its axial edges as pictured in Fig. 1. The mesh comprises 3D solid elements for a total of $44,800$ elements and $68,768$ nodes.

The finite element model of the blade is not computationally efficient and a component mode synthesis is required. Among all existing techniques, only a few offer direct access to physical displacements in the reduced order space, in which contact constraints can be fully treated, thus avoiding permanent backward and forward mappings to the physical space. The Craig-Bampton [16] technique from the fixed interface component mode synthesis family, and the Craig-Martinez [31] strategy, from the free interface component mode synthesis family are two well-known methods that keep a few physical displacements within the reduced-order space. While respective attractive features and shortcomings may be discussed, it has been shown that the Craig-Martinez is well suited for rotor/stator interaction in a two-dimensional framework [9]. However, when larger 3D models are involved, numerical stability becomes a major concern and the Craig-Bampton method seems more robust and appropriate [8].

As a consequence, the following three assumptions are adopted:

17

1. For the blade of interest, contact is anticipated on three nodes located in the leading edge, middle of the chord, and trailing edge. This is a sensitive issue since it may strongly affect the results. Simulations with an increasing number of nodes describing the contact interface (1,3,8 and 15) showed that three nodes were a good compromise between computational efficiency and accuracy. A slave contact surface in the form of a spline connected to the corresponding facing nodes is attached to the casing.

2. In the Craig-Bampton technique, the three spatial displacements of the nodes where contact is anticipated are defined as interface dof, and all other displacements are internal dof.

3. The contact matrix $\mathbf{C_{NT}}$ in Eq. (8) is constructed by assuming that the direction of sliding between the two structures is approximated by its circumferential component because of the ratio between tangential and axial components of the relative velocity.

Moreover, each patch of the B-spline surface is affected by four nodes of the casing finite element mesh. The choice is made to use three patches over the width of the casing (similarly to what is depicted in Fig. 1) and a hundred patches along its circumference to reach a total of 400 nodes supporting the B-spline surface.

5.2 Model reduction

Component mode synthesis procedures consist in subdividing a structure into non-overlapping components called substructures for which the interface dof[5] is preserved. Each substructure is then represented by a set of specific structural shapes including vibration normal modes, rigid body modes, static modes, and interface modes defining the change of variable used for the size reduction of the original problem. The dynamics of the full system are accurately captured in the low frequency spectrum, up to a precision controlled by the size of the truncated set.

5.2.1 Craig-Bampton procedure

Once the substructures are defined, the Craig-Bampton reduction basis of each substructure is composed of a truncated set of component modes and a full set constraint modes [16]:

Component modes: they are normal modes of vibration of the structural component with all interface dof constrained to feature zero-displacement. They are stored in matrix $\mathbf{\Phi_L}$.

Constraint modes: they are the sequential static responses of each component to a unit displacement of interface dof i while all its interface counterparts are fixed. This set is denoted by $\mathbf{\Phi_R}$.

For each substructure (i), the original equations of motion are projected onto the new reduced-order space such as the displacement vector $\mathbf{u}^{(i)}$ becomes:

$$\mathbf{u}^{(i)} = \mathbf{\Phi}^{(i)}\mathbf{u}_r^{(i)}$$
$$\begin{pmatrix}\mathbf{u_b}\\\mathbf{u_i}\end{pmatrix}^{(i)} = \begin{bmatrix}\mathbf{I} & \mathbf{0}\\\mathbf{\Phi_R} & \mathbf{\Phi_L}\end{bmatrix}^{(i)}\begin{pmatrix}\mathbf{u_b}\\\mathbf{q}\end{pmatrix}^{(i)} \tag{27}$$

where the number of component modes (size of $\mathbf{q}$) is substantially smaller than the number of internal physical dof (size of $\mathbf{u_i}$).

In the present study, there is a single substructure, one blade, and the respective superscript in Eq. (27) is now discarded for the sake of readability. The initial dynamic equation of the blade in the physical space:

$$\mathbf{M\ddot{u}} + \mathbf{D\dot{u}} + \mathbf{Ku} = \mathbf{F} \tag{28}$$

is transformed to:

$$\mathbf{M_r\ddot{u}_r} + \mathbf{D_r\dot{u}_r} + \mathbf{K_r u_r} = \mathbf{F_r} \tag{29}$$

where $\mathbf{X_r} = {}^t\mathbf{\Phi X\Phi}$, $\mathbf{X} \equiv \mathbf{M}, \mathbf{D}, \mathbf{K}$ and $\mathbf{F_r} = {}^t\mathbf{\Phi F}$.

---

[5]boundary or junction dof common to adjoined substructures

5.2.2 Centrifugal stiffening

While dealing with relatively stiff and small blades, a linear approximation of centrifugal stiffening may be accurate and the classical component mode synthesis techniques are convenient. However, for longer blades, centrifugal effects induce highly nonlinear stiffening stresses as well as significant variations in the geometry.

Consequently, centrifugal effects should be accounted for in the construction of the reduced-order model. This is achieved by using the polynomial expansion of the stiffness matrix introduced in [41] over a specific angular velocity range $[0; \Omega_m]$ such as:

$$\mathbf{K}(\Omega) = \mathbf{K}^0 + \Omega^2 \mathbf{K}^1 + \Omega^4 \mathbf{K}^2 \tag{30}$$

where:

$$
\begin{aligned}
\mathbf{K}^0 &= \mathbf{K}(0) \\
\mathbf{K}^1 &= \frac{1}{3\Omega_m^2}\left[16\mathbf{K}\left(\frac{\Omega_m}{2}\right) - \mathbf{K}(\Omega_m) - 15\mathbf{K}(0)\right] \\
\mathbf{K}^2 &= \frac{3}{4\Omega_m^4}\left[\mathbf{K}(\Omega_m) - 4\mathbf{K}\left(\frac{\Omega_m}{2}\right) + 3\mathbf{K}(0)\right]
\end{aligned}
\tag{31}
$$

Projection of matrix (30) through transformation (27) defined at rest is accurate for $\mathbf{K}(0) = \mathbf{K}^0$ only. Since the computation of $\mathbf{K}^1$ and $\mathbf{K}^2$ demands the calculation of stiffness matrices at $\Omega_m/2$ and Ω_m, their projection in a reduced space requires the computation of component and constraint modes at $\Omega_m/2$ and Ω_m as well. These three Craig-Bampton reduction bases defined at $\Omega = 0$, $\Omega_m/2$ and Ω_m respectively are concatenated as follows:

$$\mathbf{\Phi} = \begin{bmatrix} \mathbf{I} & \mathbf{I} & \mathbf{I} & \mathbf{0} & \mathbf{0} & \mathbf{0} \\ \mathbf{\Phi_R}(0) & \mathbf{\Phi_R}\left(\frac{\Omega_m}{2}\right) & \mathbf{\Phi_R}(\Omega_m) & \mathbf{\Phi_L}(0) & \mathbf{\Phi_L}\left(\frac{\Omega_m}{2}\right) & \mathbf{\Phi_L}(\Omega_m) \end{bmatrix} \tag{32}$$

Due to highly possible similarities in the static and component modeshapes calculated at $\Omega = 0$, $\Omega_m/2$ and Ω_m, matrix (32) is prone to rank deficiencies and is first adjusted as follows:

$$\mathbf{\Phi} = \begin{bmatrix} \mathbf{I} & \mathbf{0} & \mathbf{0} & \mathbf{0} & \mathbf{0} & \mathbf{0} \\ \mathbf{\Phi_R}(0) & \mathbf{\Phi_R}\left(\frac{\Omega_m}{2}\right) - \mathbf{\Phi_R}(0) & \mathbf{\Phi_R}(\Omega_m) - \mathbf{\Phi_R}(0) & \mathbf{\Phi_L}(0) & \mathbf{\Phi_L}\left(\frac{\Omega_m}{2}\right) & \mathbf{\Phi_L}(\Omega_m) \end{bmatrix} \tag{33}$$

This matrix is then orthonormalized through the Gram-Schmidt procedure by constructing a new set of constraint modes $\mathbf{\Psi}$ such that the *generalized* Craig-Bampton transformation matrix becomes:

$$\mathbf{\Phi} = \begin{bmatrix} \mathbf{I} & \mathbf{0} \\ \mathbf{\Phi_R}(0) & \mathbf{\Psi} \end{bmatrix} \tag{34}$$

For each angular velocity, α component modes and n constraint modes are calculated yielding a *maximum*[6] of $3n + 3\alpha$ columns in $\mathbf{\Phi}$, as reflected in Eq. (32). In the remainder, η denotes the number of columns of $\mathbf{\Psi}$ and controls the size of the reduced-order model. The latter is thus described with both physical degrees of freedom and modal coordinates similarly to the usual Craig-Bampton reduction detailed in Eq. (27). The physical degrees of freedom are required for the blade-tip contact treatment. The η modal coordinates correspond to an orthonormal basis involving component and constraint modes obtained at different angular velocities as detailed in Eq. (33). The Ω-dependent reduced-order model consistent with $\Omega \in [0; \Omega_m]$ is computed accordingly:

$$\mathbf{K}_r^0 = {}^t\mathbf{\Phi}\mathbf{K}^0\mathbf{\Phi}; \quad \mathbf{K}_r^1 = {}^t\mathbf{\Phi}\mathbf{K}^1\mathbf{\Phi}; \quad \mathbf{K}_r^2 = {}^t\mathbf{\Phi}\mathbf{K}^2\mathbf{\Phi} \tag{35}$$

yielding the global reduced stiffness matrix:

$$\mathbf{K}_r(\Omega) = \mathbf{K}_r^0 + \Omega^2\mathbf{K}_r^1 + \Omega^4\mathbf{K}_r^2 \tag{36}$$

---

[6]The Gram-Schmidt orthonormalization process may discard a few of them.

and global reduced mass matrix[7]:

$$\mathbf{M}_r = {}^t\mathbf{\Phi}\mathbf{M}\mathbf{\Phi} \tag{37}$$

As a first approach, the geometry variation due to the centrifugal effects is not accounted for. Only the centrifugal stiffening affecting the natural frequencies of the rotating bladed disk is explicitly embedded in the proposed numerical tool.

The computation of the reduced-order model of the bladed disk requires a dedicated convergence study. Component mode synthesis methods are restricted to a narrow frequency range of interest. In the present study, this is limiting since contact events are frequency-wise wideband phenomena. Nevertheless, in-depth analyses around the frequency of the first flexural mode showed that asymptotic convergence is achieved for a suitable reduction parameter η. Considering the drastic gain in computational efficiency, the proposed strategy is fully justified.

5.3 Configuration of interest

(a) case 1   (b) case 2   (c) case 3
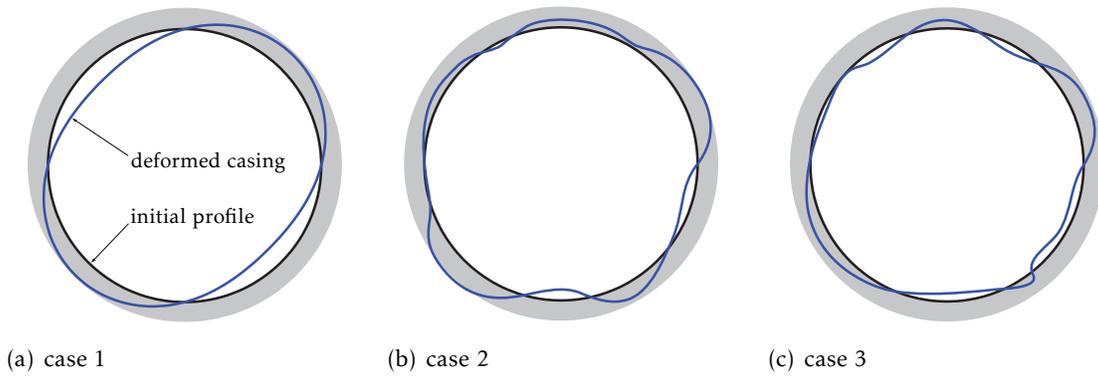
Figure 13: Magnified distortion of the casing

Contact between the blade-tip and surrounding casing is initiated by pseudo-statically distorting the latter on a chosen shape so that the initial clearance is absorbed.

Three different rigid profiles are investigated: (1) the casing is deformed along its first 2-nodal diameter free vibration mode as depicted in Fig. 13(a), (2) the shape combines both the first 2- and 5-nodal diameter free vibration modes as illustrated in Fig. 13(b), and (3) the deformation of the casing incorporates a contribution of five free vibration modes, displayed in Fig. 13(c). These scenarios are motivated by experimental observations showing that thermal gradient tend to distort the casing along a two-nodal diameter dominant shape.

For each configuration, 225 simulations are carried out over the operating range of the selected blade from $\Omega = 5$ to $\Omega = 50$. Every simulation covers twenty full revolutions of the rotor.

5.4 Time response and frequency-domain analysis

As mentioned above, a Lagrange multiplier-based method prevents possible residual penetrations. Two quantities of interest may be exploited to examine the behavior of the proposed numerical tool, namely, the distances separating the two components and the related contact forces. Blade-tip/casing distances with respect to time of the three selected interface contact nodes of the blade are depicted in Fig. 14(a) where it appears that residual penetrations cannot be distinguished.

From the interacting motion shown in Fig. 14(a), it can be observed that only one interface node comes into contact against the casing yielding the contact force displayed in Fig. 14(b) and satisfying Signorini condition $(3)_1$, positive as a convention. These results emanate from the choice of the shape exerted on the casing along the axial direction which is constant in the present study.

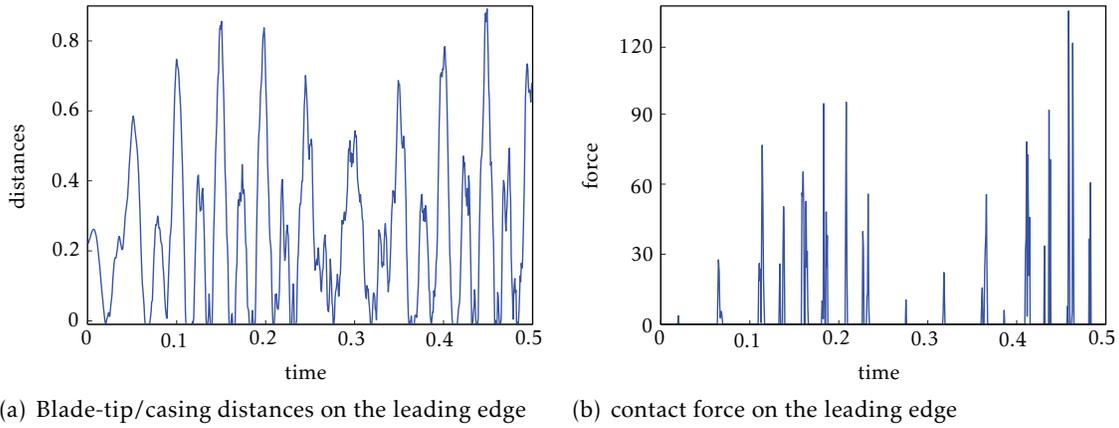[7]$\mathbf{M}_r$ implicitly depends on Ω_m through transformation matrix $\mathbf{\Phi}$.

(a) Blade-tip/casing distances on the leading edge

(b) contact force on the leading edge

Figure 14: Blade-tip/casing contact simulation (case 1, $\Omega = 35$)

(a) Time domain (steady state is reached after $t = 1.2$)
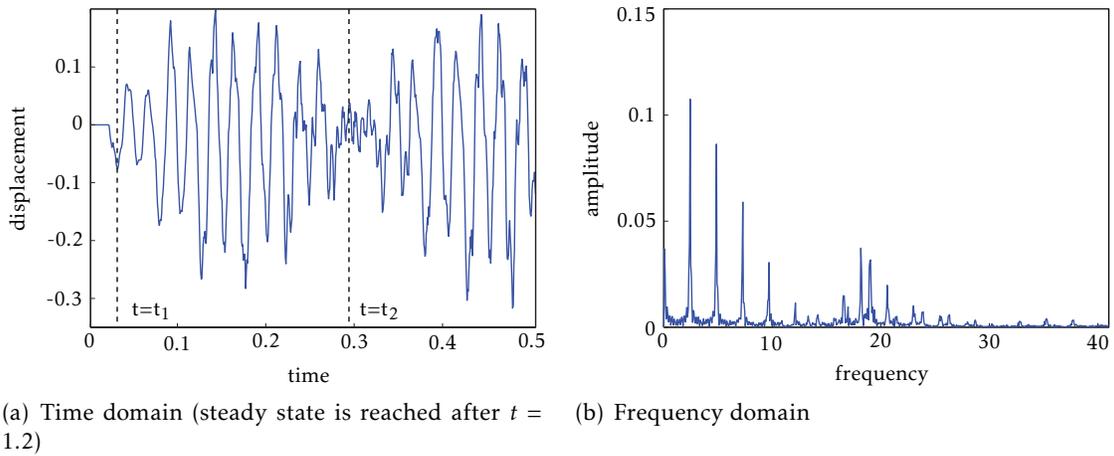

(b) Frequency domain

Figure 15: Radial displacement of the leading edge (case 1, $\Omega = 35$)

For each rotational velocity Ω, the steady-state portion of time-domain displacements is processed by the FFT for the detection of possible dangerous operating regimes involving large vibratory amplitudes. As an example, the radial displacement of the leading edge node of the blade is partially pictured in time domain in Fig. 15(a) and in frequency domain in Fig. 15(b). Other results are pictured for the three selected configurations in Fig. 16, Fig. 17 and Fig. 18, respectively, as three-dimensional frequency diagrams. For each velocity, the Fourier spectrum is truncated to low frequencies around the first natural frequency of the blade. The constant contribution in the spectrum is removed since it does not affect vibration-originated failures and fatigue-related phenomena.

First of all, engine-order harmonics $f = k f_\Omega$ are plotted for $k = 1, \ldots, 10$. The intersections of these harmonics with low natural frequencies $f = f_n$ of the blade classically define design critical velocities for turbomachines as depicted in Campbell diagrams. These critical velocities are based on linear considerations that should be generalized to nonlinear frameworks. Depending on the nature of the nonlinearity involved, this may not be straightforward. Anyway, it is known that unilateral contact conditions induce a mechanical stiffening of the contacting structures in the form of slightly increased resonance frequencies [14]. This behavior is evidenced in Figs. 16, 17 and 18 where the resonance peaks are located just above the centrifugally stiffened natural frequency of the blade that can be captured by the reduced-order model as shown by the Ω-dependent red curve $f = f_1$.

In Fig. 16, it is noteworthy to mention that significant vibratory amplitudes are detected for peaks (roughly) satisfying the condition $f = k f_\Omega$ for k even. As a matter of fact, since the casing
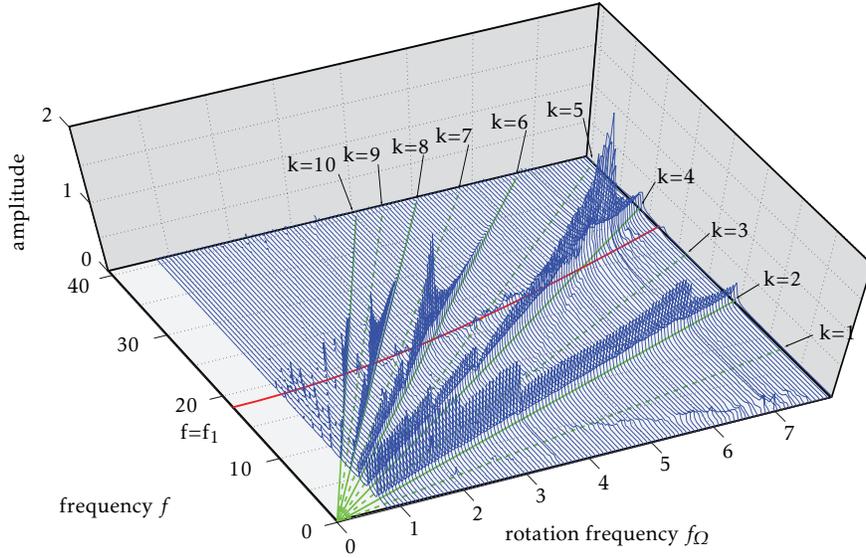
21

Figure 16: Spectrum of the radial displacement of the the leading edge node in configuration 1
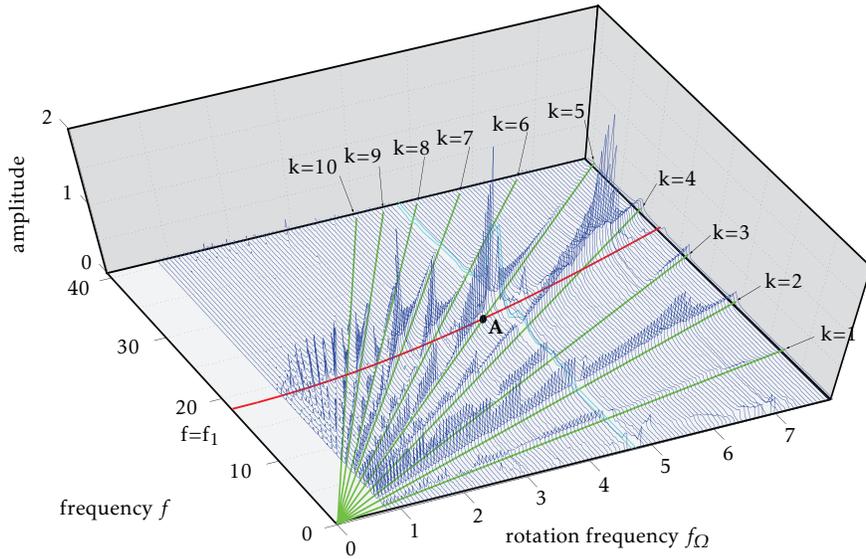

Figure 17: Spectrum of the radial displacement of the the leading edge node in configuration 2

has a two-nodal diameter static modeshape, two contact areas per revolution are privileged then yielding a synchronization of the blade response to an evenly distributed contact forcing. When odd as well as even nodal-diameter shapes are involved in the distortion of the casing, such as in Figs. 17 and. 18, resonance frequencies satisfy then $f = k f_\Omega$ for any k.

Eventhough structural damping is not negligible, for both configurations (2) and (3) (respectively depicted in Figs. 17 and 18) the system becomes mechanically unstable and divergence is observed over a range of rotational velocities: these are displayed in light blue[8]. In configuration (2), the system experiences a divergence for $f_1 \simeq 5 f_\Omega$ (highlighted by point **A** in Fig. 17). Similarly, a divergence is recognized in the third configuration for $f_1 \simeq 4 f_\Omega$ (point **B** in Fig. 18). Depending on the scenario of interaction, distinct critical velocities are predicted and nonlinear superharmonic resonances involving lower critical rotational velocities of the blade may be more problematic than previously expected.

---

[8]around $f_\Omega = 4.8$ in Fig. 17 and $f_\Omega = 6.7$ in Fig. 18
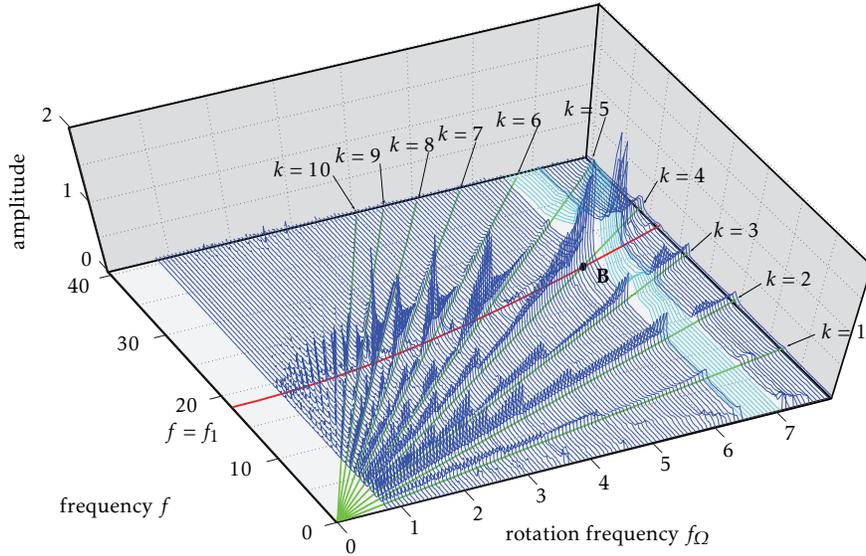
Figure 18: Spectrum of the radial displacement of the the leading edge
node in configuration 3

5.5 Contact areas

It seems interesting to look at the areas where the blade impacts the casing since repeated contact forces on confined areas of the casing can lead to a mechanical failure. Such areas for cases
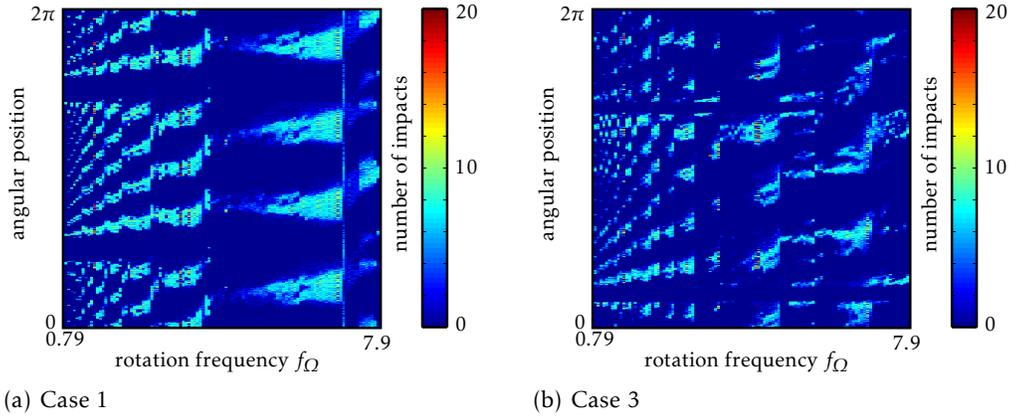

(a) Case 1

(b) Case 3

Figure 19: Contact areas between the blade leading edge and the casing
over twenty revolutions

1 and 3 are pictured in Figs. 19(a) and 19(b), respectively. The evenly distributed contact areas in Fig. 19(a) are consistent with the casing shape of Fig. 13(a) as well as with the frequency domain-results pictured in Fig. 16. Sudden jumps in the number of impacted zones can be observed versus the rotational velocity. These jumps are directly interrelated with the modal signature of the blade. For $f_\Omega \in [3.5; 7]$, the number of contact zones do not depend on the rotational velocity even though the dimension of these areas is (almost) linearly-dependent on this parameter. To the contrary, when the casing is not evenly distorted (see Fig. 13(c)), the pattern of the contact zones is unclear as shown in Fig. 19(b) with the association of several different harmonics and superharmonics as expected.

Accordingly, perfectly tuned casing profiles may lead to unfavorable high fatigue cycles (and higher abradable wear levels which are not discussed in the present work) because of the repeated contact events on localized areas over a wide range of rotational velocities.

5.6 Stresses distribution

It is also possible to monitor strains and stresses within the blade during the interaction. The identification of critical areas and the detection of structural integrity issues is a primary concern for designers and the mechanical components lifespan. To this end, numerical simulations carried out with a reduced-order model should be first transformed back into the original physical space using Eq. (27). Straightforward algebraic operations provide access to the corresponding stress field at each time step. As an example, attention is brought to the blade displacement

(a) Time $t = t_1$ (case 1, $\Omega = 35$)　　　　(b) Time $t = t_2$ (case 1, $\Omega = 35$)
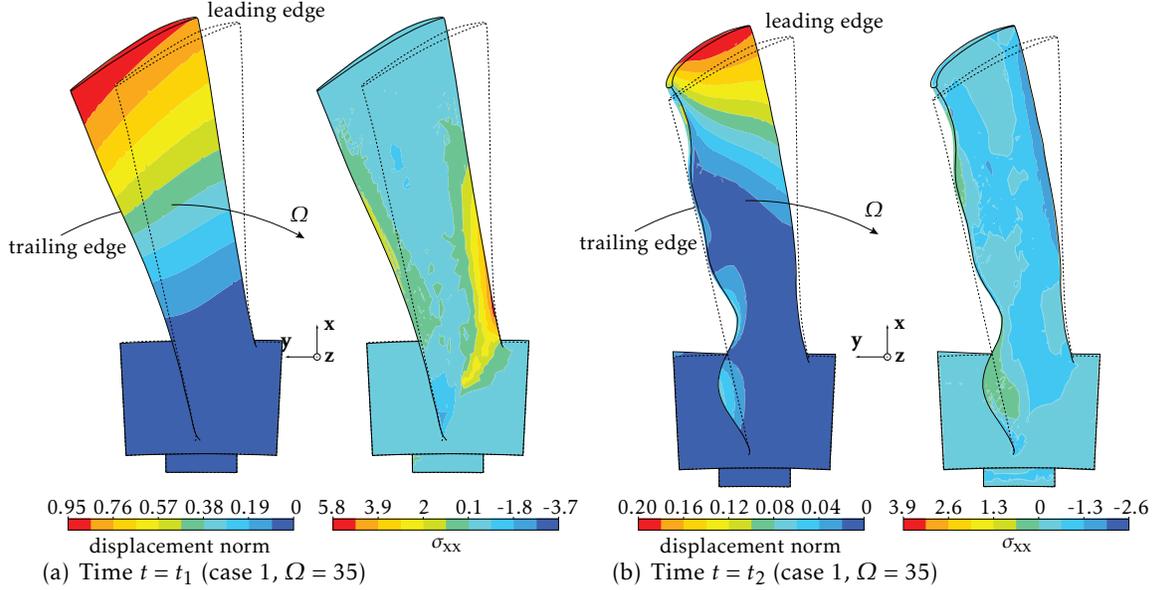
Figure 20: Displacement norm and σ_{xx} stress fields in one blade

and stress fields represented in Fig. 20 at times $t = t_1$ and $t = t_2$ in case 1 as depicted in Fig. 15(a). Time $t = t_1$ corresponds to the first contact of the blade and the casing while time $t = t_2$ corresponds to a low level of vibration over a significant period of time. One can notice in Fig. 20(a) that the blade essentially bends in a direction opposite to the rotation of the blade, as expected, motion that equally involves the contact interface nodes. This initial event induces displacements higher on the trailing edge than the leading edge. After several contacts between the blade and the casing, the blade deflects in a more complex fashion, as seen at time $t = t_2$. Indeed, the displacement and stress fields pictured in Fig. 20(b) illustrate that higher frequency modes than the usual first flexural and torsional eigenmodes are involved.

The critical areas in terms of stress levels are located on both the trailing and the leading edge predominantly around the blade root. This observation is consistent with several incident reports or experimental studies [38, 25, 44].

6 Concluding remarks

A three-dimensional contact algorithm dedicated to the study of turbomachinery structural interaction based on the forward increment Lagrange multiplier method with explicit time integration is detailed. Large sliding motions are addressed through a smoothing procedure based on a bicubic B-spline description of the contact surface that avoids the facetization phenomenon exhibited when classical linear finite elements are considered. In an industrial context, this technique advantageously allows for the use of a broader class of finite elements for the numerical analysis of the problem of interest.

In order to show the accuracy of the developed numerical tool, a comparison on a purposely designed benchmark configuration is conducted with an academic contact code implementing an implicit time-stepping solution method of the bi-potential formulation, and with a finite element commercial software package. It is shown that the results compare favorably and that

the algorithm properly preserves the energy of the whole system. This in-house code is then deployed for the analysis of a practical example dealing with an aircraft-engine rotating bladed-disk possibly in contact with a surrounding stationary casing.

A reduced-order model is first built through the use of a component mode synthesis method capable to handle centrifugal stiffening. Frequency domain diagrams of the vibratory levels emphasize the existence of numerous critical velocities to which attention should be paid. By incorporating sophisticated formulations for engineering-like usage, this numerical tool seems suitable and promising for future investigations, in the optimization discipline for instance, in order to design blades more robust to contact conditions. It also provides access to quantities of interest such as strain and stress fields within the blade as well as contact areas distribution.

Acknowledgement

[1] N. El-Abbasi, S. A. Meguid, and A. Czekanski. "On the modelling of smooth contact surfaces using cubic splines". *International Journal for Numerical Methods in Engineering* 50.4 (2001), p. 953–967.
DOI: 10.1002/(SICI)1097-0207(19990920)46:2<275::AID-NME675>3.0.CO;2-W.

[2] *ANSYS, Inc. Theory Reference*. Ansys release 10.0. Aug. 2005.

[3] F. Armero and E. Petöcz. "Formulation and analysis of conserving algorithms for dynamic contact/impact problems". *Computer Methods in Applied Mechanics and Engineering* 158 (1998), p. 269–300.
DOI: 10.1016/S0045-7825(97)00256-9.

[4] E. Arnoult. "Modélisation numérique et approche expérimentale du contact en dynamique: application au contact aubes/carter de turboréacteur". Ph.D. thesis. Nantes, France: Université de Nantes, 2000.

[5] J. S. Arora, A. I. Chahande, and J. K. Paeng. "Multiplier methods for engineering optimization". *International Journal for Numerical Methods in Engineering* 32 (1991), p. 1485–1525.
DOI: 10.1002/nme.1620320706.

[6] L. Baillet, D. Clair, H. Walter, and M. Brunet. "A 3D contact algorithm for explicit dynamic Finite Element codes applied to the ironing process". *Metal Forming 2000*. NUMISHEET. Krakov, Poland, 2000, p. 141–147.

[7] B. A. Barsky. "End conditions and boundary conditions for uniform B-spline curve and surface representations". *Computers in Industry* 3.1-2 (1982), p. 17–29. ISSN: 0166-3615.
DOI: 10.1016/0166-3615(82)90028-8.

[8] A. Batailly. "Simulation de l'interaction rotor/stator pour des turbomachines aéronautiques en configuration non-accidentelle". Ph.D. thesis. Nantes, France: École Centrale de Nantes, 2008.
OAI: tel.archives-ouvertes.fr:tel-00364945.

[9] A. Batailly, M. Legrand, P. Cartraud, and C. Pierre. "Assessment of reduced models for the detection of modal interaction through rotor stator contacts". *Journal of Sound and Vibration* 329 (2010), p. 5546–5562.
DOI: 10.1016/j.jsv.2010.07.018.

[10] Y. Bazilevs et al. "Isogeometric analysis using T-splines". *Comput. Methods Appl. Mech. Engrg.* 199 (2010), p. 229–263.
DOI: 10.1016/j.cma.2009.02.036.

[11] C. de Boor. *B(asic)-Spline Basics in Fundamental Developments of Computer-Aided Geometric Modeling*. Washington D.C.: (Piegl L., ed.) Academic Press, 1993, p. 27–49.

[12] N. Carpenter, R. Taylor, and M. Katona. "Lagrange constraints for transcient finite element surface contact". *International Journal for Numerical Methods in Engineering* 32 (1991), p. 103–128.
DOI: 10.1002/nme.1620320107.

[13] D. Chamoret, P. Saillard, A. Rassineux, and J.-M. Bergheau. "New smoothing procedures in contact mechanics". *Journal of Computational and Applied Mathematics* 168.1–2 (2004), p. 107–116.
DOI: 10.1016/j.cam.2003.06.007.

[14] F. Chu and W. Lu. "Stiffening effect of the rotor during the rotor-to-stator rub in a rotating machine". *Journal of Sound and Vibration* 308 (2007), p. 758–766.
DOI: 10.1016/j.jsv.2007.03.059.

[15] P. G. Ciarlet. *The finite element method for elliptic problems*. North-Holland, 1978.

[16] R.R. Craig and M.C.C Bampton. "Coupling of substructures for dynamic analyses". *AIAA Journal* 6.7 (1968), p. 1313–1319.

[17] A.F. Emery, J. Wolak, S. Etemad, and S.R. Choi. "An Experimental Investigation of Temperatures due to Rubbing at the Blade-Seal Interface in an Aircraft Compressor". *Wear* 91 (1983), p. 117–130.
DOI: 10.1016/0043-1648(83)90248-X.

[18] Z. Q. Feng, P. Joli, M. Cros, and B. Magnain. "The bi-potential method applied for the modeling of dynamic problems with friction". *Computational Mechanics* 36 (2005), p. 375–383.
DOI: 10.1007/s00466-005-0663-8.

[19] M. Géradin and D. Rixen. *Mechanical Vibrations*. Wiley, 1997.

[20] T.J.R. Hughes, J.A. Cottrell, and Y. Bazilevs. "Isogeometric analysis: CAD, finite elements, NURBS, exact geometry and mesh refinement". *Comput. Methods Appl. Mech. Engrg.* 194 (2005), p. 4135–4195.
DOI: 10.1016/j.cma.2004.10.008.

[21] T. J. R. Hughes, R. L. Taylor, J. L. Sackman, A. Curnier, and W. Kanoknukulchai. "A finite element method for a class of contact-impact problems". *Computer Methods in Applied Mechanics and Engineering* 8 (1976), p. 149–276.
DOI: 10.1016/0045-7825(76)90018-9.

[22] T. J. R. Hugues. "Stability, convergence and growth and decay of energy of the average acceleration method in nonlinear structural dynamics". *Computers & Structures* 6 (1976), p. 313–324.
DOI: 10.1016/0045-7949(76)90007-9.

[23] M. L. Kaplan and J. H. Heegaard. "Energy-conserving impact algorithm for the heel-strike phase of gait". *Journal of Biomechanics* 33 (2000), p. 771–775.

[24] N. Kikuchi. "Penalty/finite element approximations of a class of unilateral contact problems". *Penalty Method and Finite Element Method* (1982). ASME: New York.

[25] H. Kim. "Crack evaluation of the fourth stage blade in a low-pressure steam turbine". *Engineering Failure Analysis* 18 (3 2011), p. 907–913.
DOI: 10.1016/j.engfailanal.2010.11.004.

[26] S. K. Lahiri, J. Bonet, and J. Peraire. "A variationally consistent mesh adaptation method for explicit Lagrangian dynamics". *Int. J. Numer. Meth. Engng* 82 (2007), p. 1073–1113.
DOI: 10.1002/nme.2784.

[27] T.A. Laursen. *Computational contact and impact mechanics*. Springer, 2002.

[28] M. Legrand, C. Pierre, P. Cartraud, and J. P. Lombard. "Two-dimensional modeling of an aircraft engine structural bladed disk-casing modal interaction". *Journal of Sound and Vibration* 319.1-2 (2009), p. 366–391.
DOI: 10.1016/j.jsv.2008.06.019.
OAI: hal.archives-ouvertes.fr:hal-00328186.

[29]   W. N. Liu, G. Meschke, and H. A. Mang. "Algorithmic stabilization of FE analyses of 2D frictional contact problems with large slip". *Computer Methods in Applied Mechanics and Engineering* 192.16-18 (2003), p. 2099–2124.
DOI: 10.1016/S0045-7825(03)00252-4.

[30]   B. Magnain. "Développement d'algorithmes et d'un code de calcul pour l'étude des problèmes de l'impact et du choc". Ph.D. thesis. Évry, France: Université d'Évry-Val d'Essonne, 2006.
OAI: tel.archives-ouvertes.fr:tel-00369905.

[31]   D. R. Martinez, T. G. Carne, D. L. Gregory, and A. K. Miller. "Combined experimental/analytical modeling using component mode synthesis". *25th Structures, Structural Dynamics and Material Conference*. AIAA/ASME/ASCE/AHS. 1984, p. 140–152.

[32]   J.J. Muñoz. "Modelling unilateral frictionless contact using the null-space method and cubic B-Spline interpolation". *Computer Methods in Applied Mechanics and Engineering* 197.9-12 (2008), p. 979–993. ISSN: 0045-7825.
DOI: 10.1016/j.cma.2007.09.022.

[33]   L. Noels, L. Stainier, and J. P. Ponthot. "Simulation of crashworthiness problems with improved contact algorithms for implicit time integration". *International Journal of Impact Engineering* 21 (2006), p. 799–825.
DOI: 10.1016/j.ijimpeng.2005.04.010.

[34]   M. Ortiz. "A note on energy conservation and stability of nonlinear time-stepping algorithms". *Computers & Structures* 24 (1986), p. 167–168.
DOI: 10.1016/0045-7949(86)90346-9.

[35]   V. Padmanabhan and T. A. Laursen. "A framework for development of surface smoothing procedures in large deformation frictional contact analysis". *Finite Elements in Analysis and Design* 37 (2001), p. 173–198.
DOI: 10.1016/S0168-874X(00)00029-9.

[36]   C. Padova, J. Barton, M.G. Dunn, and S. Manwaring. "Experimental Results From Controlled Blade Tip/Shroud Rubs at Engine Speed". *Journal of Turbomachinery* 129 (2007), p. 713–723.
DOI: 10.1115/1.2720869.

[37]   M. Park, Y.H. Hwang, Y.S. Choi, and T.G. Kim. "Analysis of a J69-T-25 engine turbine blade fracture". *Engineering Failure Analysis* 9 (2002), p. 593–601.
DOI: 10.1016/S1350-6307(02)00003-1.

[38]   E. Poursaeidi and M. Salavatian. "Fatigue crack growth simulation in a generator fan blade". *Engineering Failure Analysis* 16 (2009), p. 888–898.
DOI: 10.1016/j.engfailanal.2008.08.016.

[39]   J. C. Simo and T. A. Laursen. "An augmented lagrangian treatment of contact problems involving friction". *Computers & Structures* 42.1 (1992), p. 97–116.
DOI: 10.1016/0045-7949(92)90540-G.

[40]   J. C. Simo, N. Tarnow, and K. K. Wong. "Exact energy-momentum conserving algorithms and sympletic schemes for nonlinear dynamics". *Computer Methods in Applied Mechanics and Engineering* 100 (1992), p. 63–116.
DOI: 10.1016/0045-7825(92)90115-Z.

[41]   A. Sternchüss and E. Balmès. "On the reduction of quasi-cyclic disks with variable rotation speeds". *Proceedings of the International Conference on Advanced Acoustics and Vibration Engineering (ISMA)* (2006), p. 3925–3939.

[42]   I. Temizer, P. Wriggers, and T.J.R. Hughes. "Contact treatment in isogeometric analysis with NURBS". *Comput. Methods Appl. Mech. Engrg.* 200 (2011), p. 1100–1112.
DOI: 10.1016/j.cma.2010.11.020.

[43] D. Vola, E. Pratt, M. Raous, and M. Jean. "Consistent time discretization for a dynamical contact problem and complementarity techniques". *Revue Européenne des Éléments Finis* 7 (1998), p. 149–162.

[44] L. Witek, M. Wierzbińska, and A. Poznańska. "Fracture analysis of compressor blade of a helicopter engine". *Engineering Failure Analysis* 16 (2009), p. 1616–1622. DOI: 10.1016/j.engfailanal.2008.10.022.

[45] P. Wriggers, L. Krstulovic-Opara, and J. Korelc. "Smooth C^1-interpolations for two-dimensional frictional contact problems". *International Journal for Numerical Methods in Engineering* 51.12 (2001), p. 1469–1495. DOI: 10.1002/nme.227.

[46] J. P. Wright. "Analysis of an energy-conserving time integration algorithm". *Computers & Structures* 31 (1989), p. 531–533. DOI: 10.1016/0045-7949(89)90329-5.